AIMS Bioengineering, 3(3): 362-378.
DOI: 10.3934/bioeng.2016.3.362
Received: 12 June 2016
Accepted: 01 August 2016
Published: 05 August 2016

http://www.aimspress.com/journal/Bioengineering

Research article

Characterization of fluorescent iron nanoparticles—candidates for multimodal tracking of neuronal transport

Olatunji Godo [1], Karen Gaskell [2], Gunja K. Pathak [3], Christina R. Kyrtsos [3], Sheryl H. Ehrman [4], and Sameer B. Shah [5,*]

[1] Department of Materials Science and Engineering, University of Maryland College Park, 20742, MD, USA
[2] Department of Chemistry and Biochemistry, University of Maryland, College Park, 20742, MD, USA
[3] Fischell Department of Bioengineering, University of Maryland, College Park, 20742, MD, USA
[4] Department of Chemical and Biomolecular Engineering, University of Maryland, College Park, 20742, MD, USA
[5] Departments of Orthopedic Surgery and Bioengineering, University of California, San Diego, 92093, La Jolla, CA, USA

* **Correspondence:** E-mail: sbshah@ucsd.edu; Tel: 858-822-0720.

Abstract: Magnetic nanoparticles were coated with either dextran or polyacrylic acid (PAA), and compared as potential traceable carriers for targeted intraneuronal therapeutics. Nanoparticles were fabricated using a chemical reduction method and their number mean diameter, aggregation, surface chemistry, crystal structure and magnetic properties were characterized. The crystalline core of the dextran-coated nanoparticles was Fe_3O_4, while the PAA-coated sample had an iron core. The dextran-coated iron oxide nanoparticles (DIONs) and PAA-coated iron nanoparticles (PAINs) were both stable and had a similar mean diameter of less than 10 nm. However, morphologically, the PAINs were well dispersed, while the DIONs aggregated. DIONs exhibited the presence of hysteresis and ferromagnetic properties due to aggregation, while PAINs displayed superparamagnetic behavior. Surface chemistry analysis after 2 weeks of being exposed to air indicated that DIONs oxidized to Fe_2O_3, while PAINs were composed of a metallic Fe core and a mixed oxidation state shell. Based on these analyses, we concluded that PAINs are stronger candidates for examining axonal transport, since they were less prone to aggregation, offered a stronger magnetic signal, and were less oxidized. Neurotoxicity analysis of PAINs revealed that no significant toxicity was observed compared to negative controls for concentrations up to 1 mg/ml,

thus further indicating their potential utility for biological applications. Finally, we successfully conjugated PAINs to a fluorophore, rhodamine 110 chloride, through a simple two-step reaction, demonstrating the feasibility of functionalizing PAINs. This study suggests that PAINs should be further evaluated as a candidate technology for intraneuronal diagnostics and therapy.

Keywords: nanoparticles; axonal transport; neuron; polyacrylic acid; dextran; superparamagnetic; functionalized; fluorescence

1. Introduction

A variety of signaling, nutritional, and structural proteins are transported bidirectionally within long, narrow axonal projections that connect the cell bodies and terminals of neurons [1,2]. Defects in axonal transport pathways are believed to play a role in the progression of several neurodegenerative disorders, including Alzheimer's disease, Amyotrophic lateral sclerosis (ALS), Huntington's disease, and Parkinson's disease [3,4]. However, such defects have primarily been detected in animal models of disease or post-mortem in humans. Consequently, strategies to visualize and detect defects in axonal transport *in vivo* would be of high significance.

Fluorescence and magnetic resonance imaging (MRI) are the most common modalities currently used to study axonal transport in live cells and tissue. A variety of fluorescent markers, proteins, and vital dyes enable high resolution imaging, but may only be imaged within a limited focal depth (e.g. [5,6]). Non-invasive methods such as diffusion tensor MRI (dtMRI) and functional MRI (fMRI) have been used to map neural architecture and integrity, but do not possess sufficient resolution or specificity to probe neuronal transport. Popular contrast agents such as iron oxide nanoparticles and manganese have been used to bolster the resolution of MRI, enabling the estimation of bulk rates of slow axonal transport [7,8,9]. However, these reagents in their implemented form have exhibited neurotoxicity [10,11,12]. Additionally, axonal transport within individual neurons or small bundles of neurons has not been investigated.

Given their small size, capacity for functionalization, and ability to enhance contrast, nanoparticle-based technologies remain a logical approach for high-resolution assessment of axonal transport. Gold, radio-opaque, and fluorescent particles have been monitored using various spectroscopic techniques (e.g. [13,14]), but resolutions do not approach those of magnetic resonance (MR)-based techniques. Iron-based nanoparticles are an effective contrast agent for MR, and have been successfully used for a variety of applications, including tumor cell targeting and single-cell tracking [15,16]. The apparent discrepancy between the efficacy of iron oxide particles with their neurotoxicity is likely to be resolved by selecting an appropriate surface coating [17], which can profoundly influence oxidation, localization, aggregation, and biological reactivity. Dextran in particular has been oft cited as a promising polymeric particle coating, owing to its non-reactivity and frequent use as an intracellular tracer. In fact, dextran-coated magnetite nanoparticles were intended as a marker for axonal transport almost two decades ago [18], but details on their effectiveness have not yet been reported.

Given the advantages and drawbacks of existing technologies summarized above, nanoparticles suitable for probing axonal transport should be selected based on the following design criteria: i) particles should be small enough to monitor intra-axonal movement without disrupting transport;

ii) particles should not aggregate (for the same reason as (i)); iii) particles should have a sufficiently strong magnetic signal for in vivo MRI or high-resolution superconducting quantum interference device (SQUID) imaging; iv) oxidation of particles should be minimized; v) particles should not induce neurotoxicity; vi) particles should have the capacity for functionalization, for eventual targeting or multimodality.

Our previous work yielded an intriguing candidate, PAA-coated iron nanoparticles (PAINs), with potential to meet these stringent criteria [19]. In this study, we investigated the suitability of this technology for neurological tracing through further material characterization, characterization of neurotoxicity, and comprehensive comparison to another popular magnetic technology, dextran-coated iron oxide nanoparticles (DIONs). Our data indicated that PAINs were less prone to aggregation, offered a stronger magnetic signal, and were less oxidized than DIONs. We further established that PAINs were not toxic to neuronal cells and demonstrated their capacity for functionalization by coupling them covalently to a fluorophore, enabling multimodal imaging.

2. Materials and Method

2.1. Nanoparticle Synthesis

Nanoparticles were synthesized using chemical reduction, in a protocol modified from [19]. In the first solution, $FeCl_3 \cdot 6H_2O$ (0.27 g) (Sigma-Aldrich) was dissolved in deionized (DI) water (20 ml) and mixed with a 1:10 ratio of PAA (2 ml PAA:18 ml DI H_2O) 3.5 wt% originally 35 wt% (Sigma-Aldrich). (100 µl) (0.01 M) palladium(II) chloride ReagentPlus®**,** 99% (Sigma-Aldrich) and 27–30% (500 µl) of ammonia solution (J. T. Backer) was then added to the mixture above. The second solution was prepared by dissolving (0.75 g) of sodium borohydride powder, $NaBH_4$ (Fisher Scientific) in (10 ml) of DI water. The second solution was then added to the first solution in drops under strong mixing. The addition resulted in a reaction that produced many bubbles and the reaction was expected to be complete when there were no more bubbles resulting in a dark solution (pH = 8.72). Acetone (≈200 ml) was then added to the solution and the PAA and iron nanoparticles in the form of a black gel were separated from the solution by a ~0.37 T neodymium magnet (S43046, Fisher Scientific). Nanoparticles which were coated with dextran were prepared using the same method above except that the PAA (20 ml) was replaced with (20 mg) dextran, amino, (10,000 MW) (Invitrogen) dissolved in DI H_2O (20 ml) and the resulting brown solution after the addition of $NaBH_4$ (pH = 9.30) was obtained. Concentrations of PAA and dextran were sufficient to completely coat the particles.

2.2. Nanoparticle Conjugation

0.20 g 1-(3-Dimethylaminopropyl)-3-ethylcarbodiimide (EDC) (science lab: chemicals and laboratory equipment) and 0.02 g (2-*N*-morpholinoethanesulfonic acid) (MES), low moisture content ≥99% (Sigma-Aldrich) was dissolved in 2 ml PAINs dispersed in DI water. 0.002 g Rhodamine 110 chloride dye content 75% (Sigma-Aldrich) was then added and the mixture was vortexed for 3 hours at room temperature in the dark. A magnet was then placed for 2 days under 1 ml of the mixture in a centrifuge tube to attract the nanoparticles. This enabled the separation of the conjugated PAINs from the reaction. Excess dye and unconjugated particles in the reaction not attracted to the magnet were

then removed with the use of a pipette. 1 ml of DI water was then used to resuspend the conjugated PAINs and the solution was then vortexed for a minute after which a 0.2 μm filter (Millipore) was used to for filtration before fluorescence spectroscopy and microscopy measurements.

2.3. Nanoparticle Characterization

A homogeneous solution was obtained when PAINs were dispersed in DI H_2O and the sample (3 μl) was then air-dried on a transmission electron microscope (TEM) grid (200 mesh CF200-Cu 25) (Electron Microscopy Sciences) overnight. The DIONs had to be vortexed and sonicated to obtain a well dispersed solution before being air-dried overnight on the TEM grid. Transmission electron microscope (JEM 2100 LaB6) was used to analyze both samples the following day. Energy dispersive X-ray spectroscopy (EDS) from TEM provided information on the elemental composition of the samples by detecting characteristic x-rays specific to that element. Selected area electron diffraction (SAED) patterns were also obtained with the TEM to investigate the crystallinity of the samples. Sediments were noticed 2 hours after synthesis of the DIONs so a nylon (33 mm) non-sterile filter 0.20 μm (Millipore) was used to filter the solution twice to remove the sediments prior to DLS measurements (Malvern Zetasizer Nano ZS90 particle analyzer) to obtain particle size. The PAINs were also filtered twice for consistency in measurements even though these samples had no visible sediments. Both samples were dispersed in DI H_2O and freeze dried overnight after a 24-hour period and the powder diffraction patterns of the nanoparticles using X-ray diffraction were obtained after 2 weeks with the aid of Cu *Kα* radiation (1.5406 Å) (Bruker D8 Advance powder diffractometer). Powder patterns were obtained at an angular scanning range of $2\theta = 10^{o}–75^{o}$. DIONs dispersed in DI H_2O was air-dried while the magnetic colloid containing PAA and iron nanoparticles that attached to the neodymium magnet was also air-dried and X-ray photoelectron spectroscopy (XPS) was used to analyze the surface chemistry of both samples after 2 weeks. The surface chemistry of both samples was analyzed using a Kratos AXIS 165 X-ray photoelectron spectrometer operating in hybrid mode using monochromatic Al *Kα* (1486.6 V) X-radiation at 240 W. The pressure of the instrument was at 5×10^{-8} Torr or less throughout data collection. Survey spectra and high resolution spectra were collected with pass energies of 160 eV and 20 eV respectively. Samples were mounted to the sample holder using double-sided conductive copper tape, and charge neutralization was required to minimize sample charging. All spectra were calibrated to the hydrocarbon contamination peak at 284.8 eV. Peak fitting of the C 1s and Fe 2p spectra was done using a 30% Lorentzian and 70% Gaussian peak shape after the subtraction of a Shirley background, with the aid of CasaXPS software. The C 1s spectra were fit with peaks of equal full width at half maximum (FWHM). The gels, which attached to the neodymium magnet for both samples, were air dried and prepared into powder form. The samples were put in a sample holder cup (LakeShore Cryotronics, Inc) and the magnetic properties of the samples were determined using a Lakeshore 7400 Series vibrating sample magnetometer (VSM).

2.4. Cytotoxicity

Confluent neuroblastoma cells (N2a, ATCC) were exposed to iron nanoparticles dispersed in supplemented DMEM culture media at concentrations (10 μg/mL to 10 mg/mL) for 1 hour. Untreated cells were used as the positive control, while cells exposed to 70% ethanol were the

negative control. Following the 1 hour treatment period, cells were rinsed with PBS three times to remove excess nanoparticles remaining. An MTT assay (4890-025-K, R&D Systems) was then performed and absorbance measured on a plate reader at 590 nm and 670 nm.

2.5. Fluorescence Spectroscopy and Microscopy

Conjugated PAINs dispersed in DI water were passed through a 0.2 μm filter (Millipore) before obtaining the absorption spectrum. A Shimadzu 2401-PC spectrophotometer was used in measuring the optical absorbance over the spectral range of 190–820 nm in a 1 mm optical path length quartz cell (Milli-Q water blank). Fluorescence spectrum at the excitation wavelength of 497 nm was obtained with AB2 Luminescence Spectrometer in a 1-cm quartz cell with Milli-Q water as blank. SpectraMax® M5 Multi-Mode Microplate Reader was used to compare the fluorescence intensities of the conjugated and unconjugated PAINs using SoftMax® Pro Data Acquisition & Analysis Software. Fluorescence intensity readings of 3 wells of a Microplate were averaged for the conjugated PAINs and the control (unconjugated PAINs) and the excitation/emission wavelengths were set at 485/590 nm during measurements. Microscopic images were obtained using a Nikon TE-2000E inverted microscope with a 10x/0.3 NA phase contrast/fluorescence objective (0.65 μm/pixel), and exposure times were 7 ms for the DIC channel and 200 ms for the 572 nm fluorescent channel.

2.6. Statistical Analysis

Means were compared using two-tailed heteroscedastic t-test. Significance of differences between means were tested based on type I error $\alpha = 0.05$ and a minimum power = 0.8 ($\beta = 0.2$).

3. Results

3.1. Characterization of Nanoparticle Size and Tendency to Aggregate

Dextran- and PAA-coated nanoparticles were synthesized in parallel using chemical reduction, based on protocols modified from our initial synthesis of PAINs [19]. We first tested whether PAINS and DIONS were of appropriate geometry to move through axons, both in terms of their tendency for aggregation and individual particle diameters. Qualitatively, sediments were noted two hours after synthesis of the DIONs (Figure 1a), while PAINs remained well-dispersed two hours after sample preparation (Figure 1b). In preparation for TEM, 2 ml of both samples were diluted, vortexed and left overnight. Again, sediments were observed in the diluted sample of DIONs (Figure 1c), while the PAINs remained well-dispersed (Figure 1d). TEM images were consistent with these observations, revealing that DIONs appeared to cluster or aggregate (Figure 1e), while PAINs remained dispersed (Figure 1f).

Despite differences in their tendency to aggregate, size distributions were not statistically different between DIONs and PAINs. Based on analysis of TEM micrographs, individual DIONs had a number mean particle diameter of 5.0 ± 0.9 nm (mean ± standard deviation; Figure 1g), while PAINs had a number mean diameter of 4.0 ± 0.8 nm (Figure 1h). DLS analysis was consistent with particle diameters from TEM, and revealed a similar particle size distribution for both DIONs and PAINs (Figures 1i–j). The number mean diameter for the DIONs (Figure 1i) was ≈6 nm with a

polydispersity index of 0.43 while PAINs (Figure 1j) had a slightly narrower number mean diameter of ≈5 nm with a polydispersity index of 0.36. It should be noted that a 0.20 μm filter was used to filter the DIONs solution twice, to remove aggregates prior to DLS measurements. PAINs were also filtered twice for consistency, even though theses samples had no visible sediments. The pH of both samples was stable and did not increase after a two-month period.

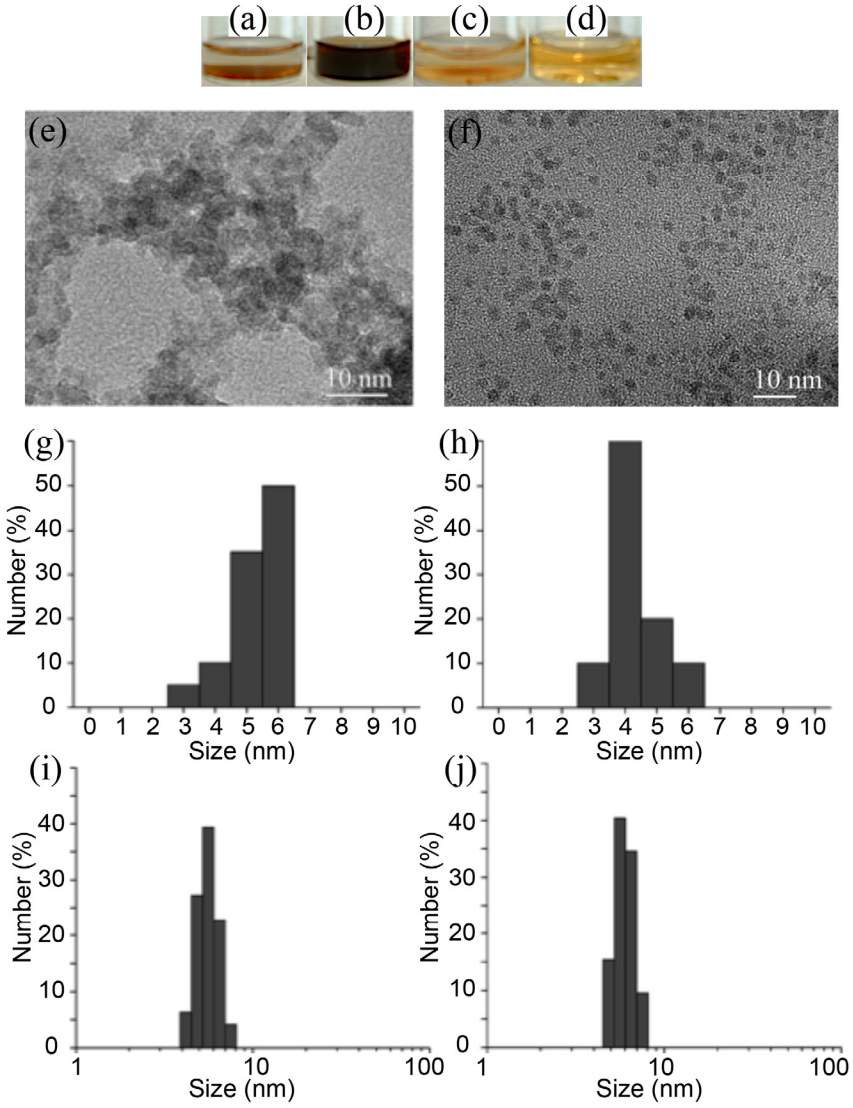

Figure 1. (a) DIONs two hours after preparation. (b) PAINs two hours after preparation. (c) Sediments were noticed when diluted DIONs were left overnight. (d) No sediments were noticed when diluted PAINs were left overnight. (e) A representative TEM image of DIONs illustrates their tendency for aggregation. (f) A representative TEM image shows PAINs are well-dispersed. (g) Distribution of diameters for DIONs based on TEM. The mean diameter of individual DIONs is 5 nm. (h) Distribution of diameters for PAINs based on TEM. The mean diameter of PAINs is 4 nm. PAINs and DIONs were assumed to be spheres for analysis of geometry. DLS analysis shows (i) DIONs are more polydispersed with wider size distribution. (j) PAINs have a narrower size distribution. A 200 nm polystyrene bead standard was run before each measurement for calibration.

3.2. Characterization of Nanoparticle Magnetic Properties

We next examined the magnetic properties of each type of particle at room temperature (25 °C). The saturation magnetizations, Ms, at 300 K were 20.0 emu/g for the DIONs and 64.5 emu/g for the PAINs (Figure 2a, 2b). DIONs also showed the presence of hysteresis, had a remanence of 1.83 emu/g and coercivity of 74.7 Oe. In contrast, PAINs displayed effectively zero remanence and coercivity, and exhibited superparamagnetic behavior, consistent with their efficient dispersion. Since PAINs exhibited superparamagnetism at room temperature, they were regarded as huge molecules and fit to the classical Langevin Function to determine the magnetic moment of each particle and the magnetic particle size, assuming that the nanoparticles were composed of single magnetic domains and were of equal size [20,21]. The appropriate Langevin function that describes superparamagnetic behavior is

$$L(x) = \coth x - (1/x) \tag{1}$$

where $x = \mu H/kBT$, μ (= MsV) is the particle magnetic moment, H is the applied magnetic field, kB is Boltzmann constant, T is the absolute temperature, Ms is the bulk saturation magnetization and V is the particle volume. Nonlinear least squares was used to fit the experimental data from the M-H curve to equation 1. The strong correlation (R^2 = 0.999) indicates that the Langevin function describes the data satisfactorily (Figure 2b). Therefore, the particles are super-paramagnetic and it can be inferred that there is insignificant magnetic interaction between the PAINs [22]. The average magnetic moment per particle obtained from the fit was 1905.9 μB and a particle size of 4.0 nm (using ρ = 7.87 g/cm^3 Fe [23]), which is consistent with results from TEM and DLS analysis.

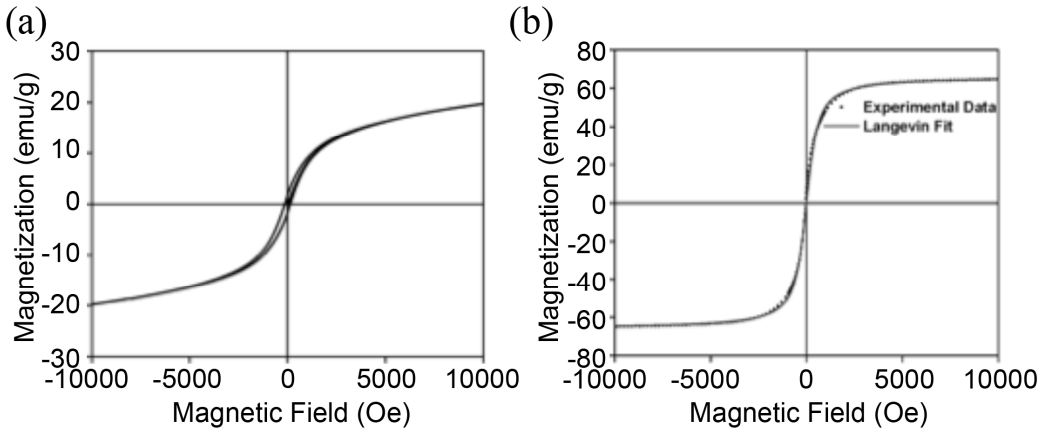

Figure 2. Magnetization curves at room temperature (a) hysteresis loop of DIONs (b) PAINs have zero remanence and coercivity and the solid line is the classical Langevin function fit, which is consistent with experimental data.

3.3. Characterization of Nanoparticle Composition and Structure

We next characterized and compared the composition and structure of DIONs and PAINs using several techniques. The EDS spectra (Figure S1) of both the DIONs and the PAINs clearly showed the elements C, O, and Fe, indicating the presence of polymer and iron in each.

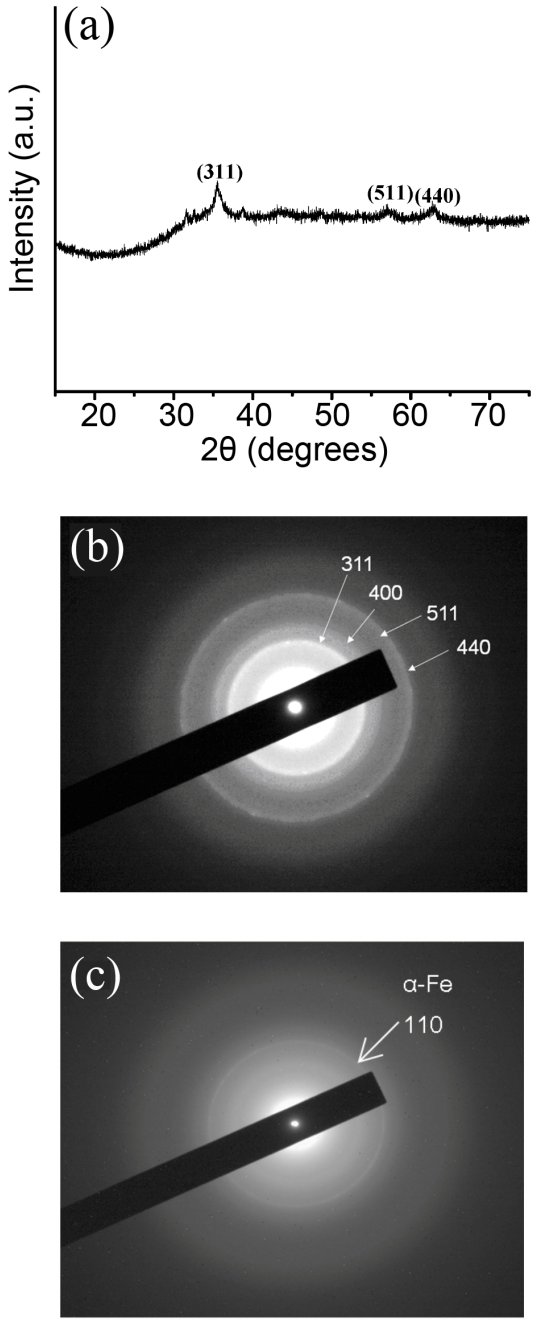

Figure 3. Comparison of diffraction patterns (a) Indexed XRD pattern of DIONs, (b) SAED pattern of DIONs agrees with XRD, (c) SAED of PAINs showing α-Fe diffraction ring.

The XRD pattern of the DIONs (Figure 3a) with d-spacings 0.2525 nm, 0.1614 nm and 0.1476 nm is indexed by a face-centered cubic magnetite crystal structure, Fe_3O_4 with diffraction peaks at (311), (511) and (440) and lattice parameter, a = 0.8378 nm, in agreement with Joint Committee on Powder Diffraction Standards (JCPDS) file No. 19-0629. Diffraction rings from the SAED of the DIONs (Figure 3b), are consistent with the d-spacings from the XRD. The SAED pattern of the PAINs (Figure 3c) was typical of all the crystalline regions in the sample and indicated the presence of body-centered cubic metallic Fe with interplanar spacing 0.2018 nm corresponding to

the (110) crystal plane, which agrees with JCPDS file No. 6-696 and our previous characterization [19]. The XRD pattern of PAINs had no crystalline peaks (Figure S2), a likely consequence of the low concentration of iron in the sample, high background scattering due to the presence of amorphous phases, or the strong fluorescent scattering of iron when using copper radiation. A lack of peaks from XRD patterns have also been reported in literature for polymer-coated iron nanoparticles [24].

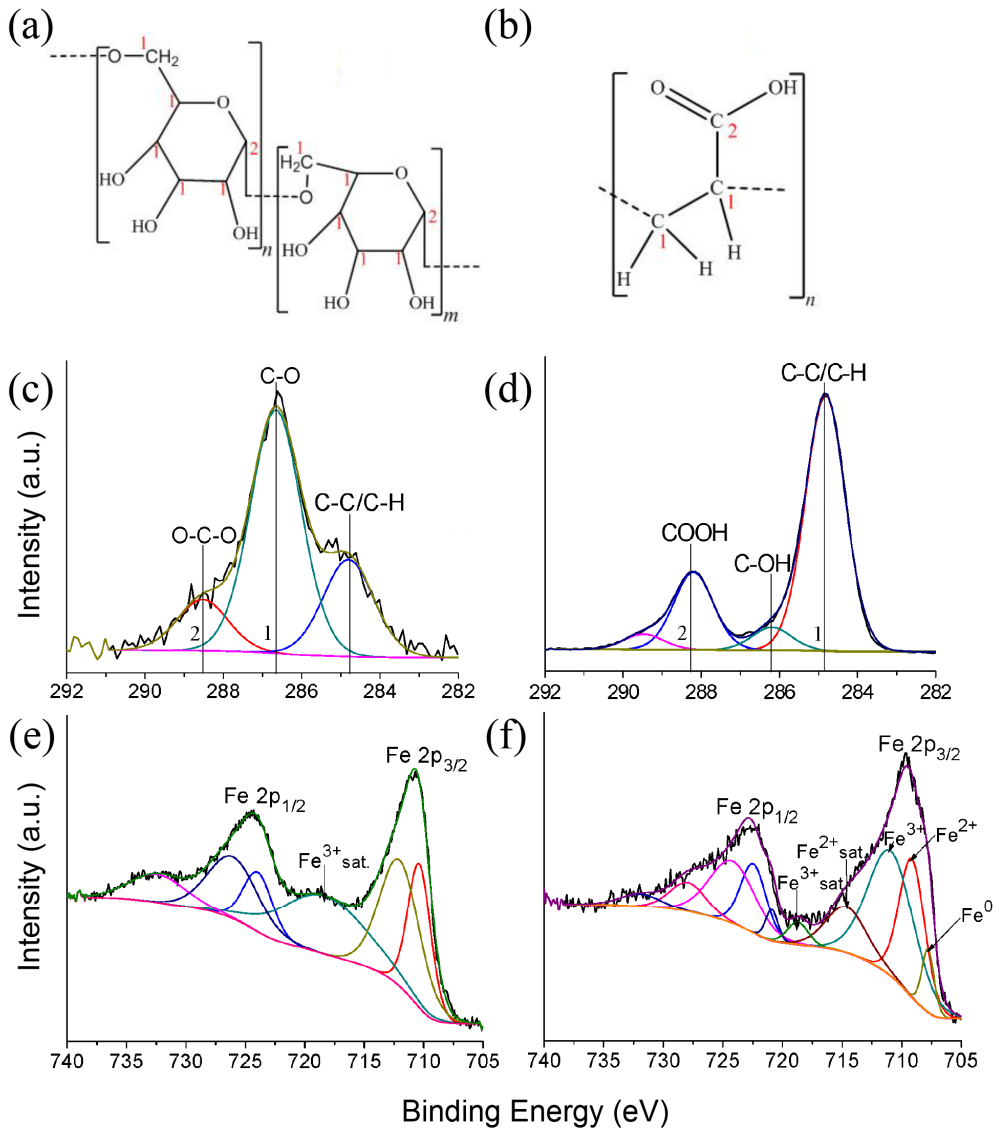

Figure 4. (a) structural representation of dextran, (b) structural representation of PAA (numbers correspond to XPS peaks). XPS spectras: (c) C 1s spectrum of DIONs, (d) C 1s spectrum of PAINs, (e) Fe 2p spectrum of DIONs and (f) Fe 2p spectrum of PAINs.

XPS analysis of the C 1s spectra was used to verify the presence of dextran and PAA (structural representation, Figure 4a, 4b) on the surface of the nanoparticles and the Fe 2p spectra were used in determining the oxidation state. C 1s spectrum of the DIONs (Figure 4c) showed peaks attributable to O–C–O at 288.5 eV and C–O at 286.7 eV with a 1:5 area ratio respectively, consistent with the

molecular structure of dextran (Figure 4a, [25]).The C–C/C–H at 284.8 eV is due to hydrocarbon contamination from the atmosphere and is used as an internal calibrant. The C 1s spectrum of the PAINs in Figure 4d shows the characteristic carbon functionalities in PAA, COOH at 288.2 eV, C–OH at 286.2 eV and C–C/C–H at 284.8 eV (Figure 4b, [26]). There was also an additional peak at 289.5 eV consistent with of CO_3^{2-}, due to a small amount of iron carbonate, confirmed by Time-of-Flight Secondary Ion Mass Spectrometry (supporting information, Figure S3). The Fe 2p spectrum for DIONs (Figure 4e) was consistent with Fe_2O_3 having a characteristic spin-orbit doublet, with the Fe $2p_{3/2}$ at 710.8 eV, spin orbit splitting of 13.6 eV, and an Fe^{3+} shakeup satellite at 718.7 eV, 7.9 eV higher than the Fe $2p_{3/2}$ peak. The Fe 2p spectrum for the PAINs (Figure 4f) revealed a complex mixture of iron oxidation states. The spectrum was fit with a pair of spin orbit split peaks of equal FWHM, a fixed separation of 13.3 eV ($Fe^{2+, 3+}$), 13.1 eV (Fe^0) and a fixed area ratio of 1:0.5 for the Fe $2p_{3/2}$ and Fe $2p_{1/2}$ components, respectively. Additionally for Fe^{2+} and Fe^{3+} components a corresponding shake-up satellite peak was also added at 5.5 eV and 7.8 eV, respectively, to higher binding energy than the 3/2 component. It was found that three spin-orbit split pairs were required for a good fit, corresponding to Fe^0 (707.8 eV), Fe^{2+} (709.2 eV) and Fe^{3+} (711.1 eV). These results are consistent with a nanoparticle having a metallic core and a mixed oxidation state shell. It is likely that Fe_3O_4 is present, however the Fe 2p region is not consistent with pure Fe_3O_4 and probably also contains small amounts of amorphous FeO and Fe_2O_3. The binding energy position of the metallic iron, 707.8 eV is slightly higher than the ≈707.2 eV reported for bulk iron in literature. This is due to the size of the nanoparticles ≈5 nm or less; this "size effect" has been reported [27].

Collectively, XPS results agree with crystal structure determination through SAED and XRD. Oxidation of Fe results in phase changes from Fe to FeO to Fe_3O_4 to Fe_2O_3.[28] It has also been reported that iron nanoparticles oxidize in a process composed of two different stages [29]. The initial oxidation occurs immediately after particles are exposed to air, while oxygen diffusion during the second stage could be slower. For DIONs, the Fe_3O_4 crystallite observed through electron diffraction after being air-dried overnight on the TEM grid had substantially oxidized to Fe_2O_3 over the course of two weeks prior to XPS analysis. In contrast, though, PAINs revealed a variety of phases of pure and oxidized iron, with little oxidation beyond Fe_3O_4 during the same period.

3.4. Neurocompatibility and Functionalization of PAINs

Based on head-to-head comparisons of size, aggregation, magnetic properties, structure, and tendency to oxidize, PAINs were by each criterion more appropriate for our intended application of tracking neuronal transport. Consequently, we used this class of nanoparticles for the remainder of the study. We first added PAINs to neuronal cells at varying concentrations, and performed an MTT (3-(4,5-dimethylthiazol-2-yl)-2,5-diphenyltetrazolium bromide) assay (Figure 5) to examine enzymatic activity as a surrogate for neurotoxicity (n = 3–4 per group). For concentrations up to 1 mg/ml, no significant toxicity was observed compared to negative controls; only at the high concentration of 10 mg/ml was toxicity observed.

Finally, we tested the capacity of PAINs for functionalization by conjugating PAINs to rhodamine 110 chloride dye, a nontoxic fluorophore that would allow us to both observe synthesized particles through fluorescence imaging as well as track particles in cultured cells, towards the eventual validation of the implementation of PAINs in vivo. The presence of COOH functional groups on the surface of the PAINs (Figure 4d) enabled the conjugation of rhodamine dye to the

particles through an (1-[3-(dimethylaminopropyl)-3-ethylcarbodiimidehydrochloride (EDC) intermediary in a (2-*N*-morpholinoethanesulfonic acid) (MES) buffer that activated the COOH groups. Fluorescence microscopy (Figure 6) of magnetically separated particles shows that there was successful binding of the dye with the surface of the PAINs and the excitation and emission peaks were located at 497 nm and 522 nm respectively through fluorescence spectroscopy. Fluorescently conjugated and unconjugated nanoparticles were then compared by fluorescence spectroscopy, again after magnetic separation. As expected, average fluorescence intensities were dramatically and significantly higher for conjugated PAINs (mean ± standard deviation: 13576 ± 2445 vs. 1.05 ± 0.28; $p < 0.01$, $n = 3$), confirming their fluorescent properties.

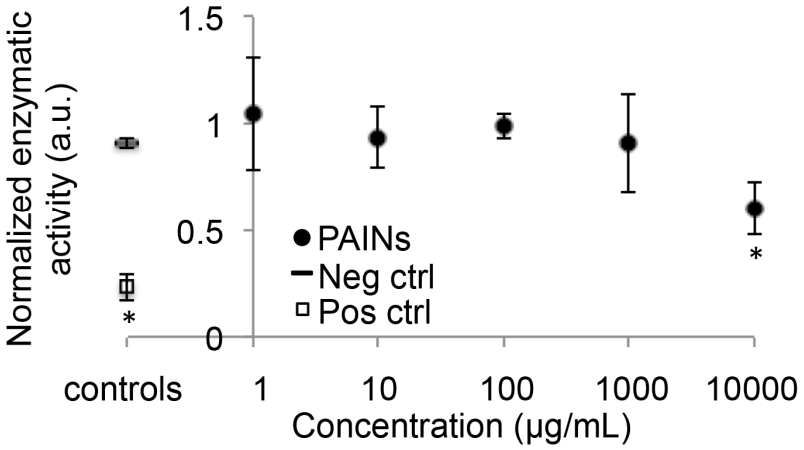

Figure 5. MTT assay reveals that there is no metabolic impact of adding PAINs to neuronal cells at concentrations 1 mg/ml and lower. No nanoparticles were added in the negative control. Ethanol was used as a positive control. * indicates $p < 0.05$ by t-test (positive control vs. negative control, 10000 µg/ml vs. negative control).

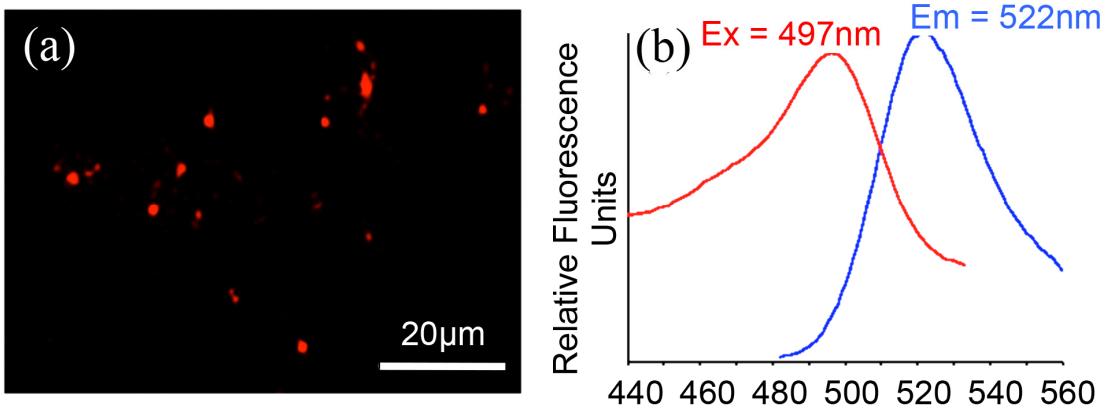

Figure 6. (a) Fluorescence microscopy image of rhodamine functionalized PAINs. Brightness and contrast have been enhanced for visibility, and thus actual dimensions may be slightly distorted. (b) Excitation and emission wavelength of conjugated PAINs obtained from fluorescence spectroscopy.

4. Discussion

In this work, we comprehensively compared the potential of PAINs and DIONS as intraneuronal tracers, based on size, tendency to aggregate, magnetic properties, and oxidative susceptibility. We further tested PAIN biocompatibility and capacity for functionalization. This work advances previous studies of PAA- and dextran-based particles by (i) more comprehensive characterization of parameters relevant to axonal tracing; (ii) direct comparison between PAINs and DIONs synthesized in parallel; (iii) demonstration of functionalization and neurocompatibility of PAINs. Based on our findings, PAINs represent a promising nanoparticle technology for monitoring axonal transport.

4.1. Comparison of PAINs and DIONs

Consistent with previous studies, including our initial fabrication and characterization of PAINs, PAINs and DIONs were both sufficiently small to move through axons (Figure 1; [19]). However, PAINs were less prone to aggregation compared to DIONs. Aggregation of dextran-coated nanoparticles have been reported previously [30,31], and may reflect differences between DIONs and PAINs in zeta potential at basic pH. The alkalinity of PAINs dispersed in water resulted in a strongly negative zeta potential, leading to electrostatic and steric repulsion between the PAINs, thereby preventing aggregation [32]. In contrast, at basic pH = 9 the zeta potential of DIONs is only slightly negative ≈ ±10 mV [33], leading to weaker (if any) repulsion, and thus an increased tendency for aggregation. The pH of both samples was stable and did not increase after a two-month period, consistent with previous reports of the stability of dextran-coated particles [32].

Measured saturation magnetizations for DIONs and PAINs (Figure 2) were of the same order of magnitude as reported for other reported dextran [30] or PAA [34] coated magnetic particles, but slightly lower than that of bulk magnetite (92 emu/g) [23] or bulk iron (218 emu/g)[23]. This difference may simply reflect the amount of iron/iron oxide in the sample compared to the amount of polymer coating present. Alternately, the surface formation of a magnetically dead layer could also induce a weaker magnetic moment [24,35]. Unlike PAINs, which appeared to be superparamagnetic (Figure 2), DIONs showed hysteresis, and thus, ferromagnetic behavior, likely due to agglomeration of nanoparticles [36].

Characterization of the composition and structure of PAINs and DIONs was performed using XPS, SAED, and XRD (Figures 3–4). Findings for each particle type were internally consistent, in agreement with previous characterization of similar (though not identical) materials [25,26,37], and revealed interesting differences in material and chemical properties. These detailed analyses suggested that though both PAINs and DIONs were of predictable and consistent crystalline core composition, PAINs were less susceptible to surface oxidation.

Based on material characterization, PAINs were by each criterion more appropriate than DIONs for our intended application of tracking neuronal transport. We confirmed their suitability for interactions with neurons by establishing low levels of neurotoxicity (Figure 5), comparable to those for dextran-coated particles [17]. Finally, PAINs revealed capacity for functionalization, based on their conjugation to a fluorophore via an EDC linker. This result should be viewed with caution, given the possibility of low levels of aggregation during the conjugation process, but provides a promising preview of multimodality.

4.2. Comparison of PAINs to Other Candidates for Probing Axonal Transport

Recent development of a silica nanoparticle highlighted the relevance of axonal transport as a therapeutic target for a number of neurodegenerative diseases, and the design constraints on neuronal targeting [38]. Development of diagnostic methods for transport dysfunction faces similar challenges. Nanoparticles used as contrast agents for MR primarily, but not exclusively, incorporate iron oxide (e.g. [13,15,39,40]). Many of these are paramagnetic (PIONs) or superparamagnetic (SPIONs), and have been used for mapping neural architecture, identifying biological targets such as tumors, and tracking implanted cells (e.g., but not limited to, [13,15,41–45]). Internalized iron oxide nanoparticles have been found in endosomes [46], which are transported bidirectionally within the axon [47–50]. However, uncoated SPIONs have been shown to have dose-dependent cytotoxicity [12].

Altering the surface chemistry or coating nanoparticles or quantum dots with surfactants, polymers, inorganic molecules, or biological molecules such as antibodies and proteins [35] have decreased their acute cytotoxicity, and also allow precise control over nanoparticle function and localization. Such manipulations have proven effective for preventing aggregation, drug delivery to normal and pathological targets within the nervous system, crossing the blood-brain barrier, tracking cells or facilitating multi-modal imaging (e.g. [15,51–58]. However, many functionalized particles continue to disrupt the function of neuronal cells, as revealed by assays testing viability, cell detachment, cytoskeletal disruption, vacuolization, and production of reactive oxygen species (ROS) [11,12,59,60,61]. Thus, of existing strategies, a limited subset of potential candidates exist. The most intriguing magnetic markers for axonal transport are fluorescent, radio-opaque, and paramagnetic CdS: Mn/ZnS quantum dots [58] and dextran-coated magnetite nanoparticles [9,18]. The former has not been tested with neurons, but requires extensive fabrication protocols, somewhat diminishing its potential. The latter, in fact, was intended as a marker for axonal transport. Our results with dextran-coated iron oxide particles raise the possibility of aggregation, though the use of carboxymethyl dextran may counteract this phenomenon [62]. In either case, the efficacy of dextran-coated magnetite nevertheless remains to be formally tested.

It should be noted that the scope of this study was limited to a comprehensive material characterization of the nanoparticles, and assessment of a minimum set of geometric and biocompatibility parameters required to confirm the potential of nanoparticles for tracking intraneuronal transport. A more comprehensive set of studies will be required in cultured cells and in vivo, where features such as efficiency of uptake by neurons, quantitative transport tracking, and magnetic tracking may be assessed.

5. Conclusions

Based on their characterization within this study and comparison of its key features with existing technologies, PAINs offer a promising strategy for magnetic monitoring of intraneuronal transport, and should be evaluated as a candidate technology for intraneuronal diagnostics and therapy. PAINs also hold broader promise for additional neurological or biomedical applications, given the generality of many of the particle design criteria posed for assessing axonal transport.

Acknowledgements

This work was supported by the National Science Foundation funded LSAMP program research scholarship (OG), L-3 Communications research scholarship (OG) and the Fischell Department of Bioengineering at the University of Maryland (SBS). We acknowledge the support of the Maryland NanoCenter and its NispLab, including Dr. Manfred Wuttig, Li-Chung Lai, Yemei Han, and Yueying Liu. The NispLab is supported in part by the NSF as a MRSEC Shared Experimental Facility. We are also grateful to Andrea A. Andrew and Neil V. Blough for assistance with fluorescence spectroscopy.

Conflict of Interest

All authors declare no conflicts of interest in this paper.

References

1. Goldstein LS, Yang Z (2000) Microtubule-based transport systems in neurons: the roles of kinesins and dyneins. *Annu Rev Neurosci* 23: 39–71.
2. Hirokawa N, Takemura R (2004) Molecular motors in neuronal development, intracellular transport and diseases. *Curr Opin Neurobiol* 14: 564–573.
3. Duncan JE, Goldstein LS (2006) The genetics of axonal transport and axonal transport disorders. *PLoS Genet* 2: e124.
4. Chevalier-Larsen E, Holzbaur EL (2006) Axonal transport and neurodegenerative disease. *Biochim Biophys Acta* 1762: 1094–1108.
5. Misgeld T, Kerschensteiner M, Bareyre FM, et al. (2007) Imaging axonal transport of mitochondria in vivo. *Nat Methods* 4: 559–561.
6. Kaether C, Skehel P, Dotti CG (2000) Axonal membrane proteins are transported in distinct carriers: a two-color video microscopy study in cultured hippocampal neurons. *Mol Biol Cell* 11: 1213–1224.
7. Enochs WS, Schaffer B, Bhide PG, et al. (1993) MR imaging of slow axonal transport in vivo. *Exp Neurol* 123: 235–242.
8. Petropoulos AE, Schaffer BK, Cheney ML, et al. (1995) MR imaging of neuronal transport in the guinea pig facial nerve: initial findings. *Acta Otolaryngol* 115: 512–516.
9. Filler AG, Bell BA (1992) Axonal transport, imaging, and the diagnosis of nerve compression. *Br J Neurosurg* 6: 293–295.
10. Thuen M, Berry M, Pedersen TB, et al. (2008) Manganese-enhanced MRI of the rat visual pathway: acute neural toxicity, contrast enhancement, axon resolution, axonal transport, and clearance of Mn^{2+}. *J Magn Reson Imaging* 28: 855–865.
11. Hussain SM, Javorina AK, Schrand AM, et al. (2006) The interaction of manganese nanoparticles with PC-12 cells induces dopamine depletion. *Toxicol Sci* 92: 456–463.
12. Pisanic TR 2nd, Blackwell JD, Shubayev VI, et al. (2007) Nanotoxicity of iron oxide nanoparticle internalization in growing neurons. *Biomaterials* 28: 2572–2581.
13. Couillard-Despres S, Finkl R, Winner B, et al. (2008) In vivo optical imaging of neurogenesis: watching new neurons in the intact brain. *Mol Imaging* 7: 28–34.

14. Choi JS, Park JC, Nah H, et al. (2008) A hybrid nanoparticle probe for dual-modality positron emission tomography and magnetic resonance imaging. *Angew Chem Int Ed Engl* 47: 6259–6262.
15. Focke A, Schwarz S, Foerschler A, et al. (2008) Labeling of human neural precursor cells using ferromagnetic nanoparticles. *Magn Reson Med* 60: 1321–1328.
16. Townsend SA, Evrony GD, Gu FX, et al. (2007) Tetanus toxin C fragment-conjugated nanoparticles for targeted drug delivery to neurons. *Biomaterials* 28: 5176–5184.
17. Rivet CJ, Yuan Y, Borca-Tasciuc DA, et al. (2012) Altering iron oxide nanoparticle surface properties induce cortical neuron cytotoxicity. *Chem Res Toxicol* 25: 153–161.
18. Filler AG (1994) Axonal transport and MR imaging: prospects for contrast agent development. *J Magn Reson Imaging* 4: 259–267.
19. Huang KC, Ehrman SH (2007) Synthesis of iron nanoparticles via chemical reduction with palladium ion seeds. *Langmuir* 23: 1419–1426.
20. Bean CP, Jacobs IS (1956) Magnetic granulometry and super-paramagnetism. *J Appl Phys* 27: 1448–1452.
21. Chantrell RW, Popplewell J, Charles SW (1978) Measurements of particle-size distribution parameters in ferrofluids. *Ieee T Magn* 14: 975–977.
22. Yatsuya S, Hayashi T, Akoh H, et al. (1978) Magnetic-properties of extremely fine particles of iron prepared by vacuum evaporation on running oil substrate. *Jpn J Appl Phys* 17: 355–359.
23. Cullity BD (1972) Introduction to magnetic materials. New York: Addison-Wiley.
24. Burke NAD, Stover HDH, Dawson FP (2002) Magnetic nanocomposites: Preparation and characterization of polymer-coated iron nanoparticles. *Chem Mater* 14: 4752–4761.
25. Frazier RA, Davies MC, Matthijs G, et al. (1997) In situ surface plasmon resonance analysis of dextran monolayer degradation by dextranase. *Langmuir* 13: 7115–7120.
26. Lan Y, Cheng C, Zhang SZ, et al. (2011) Plasma-induced Styrene Grafting onto the Surface of Polytetrafluoroethylene Powder for Proton Exchange Membrane Application. *Plasma Sci Technol* 13: 604–607.
27. Shanmugam S, Viswanathan B, Varadarajan TK (2006) A novel single step chemical route for noble metal nanoparticles embedded organic-inorganic composite films. *Mater Chem Phys* 95: 51–55.
28. Jung HI, Huh SH, Oh SJ, et al. (1999) Oxidation enthalpy of 6 nm Fe clusters. *J Korean Phys Soc* 35: 265–267.
29. Simeonidis K, Mourdikoudis S, Tsiaoussis I, et al. (2007) Oxidation process of Fe nanoparticles. *Mod Phys Lett B* 21: 1143–1151.
30. Morales MP, Bomati-Miguel O, de Alejo RP, et al. (2003) Contrast agents for MRI based on iron oxide nanoparticles prepared by laser pyrolysis. *J Magn Magn Mater* 266: 102–109.
31. Hong RY, Li JH, Qu JM, et al. (2009) Preparation and characterization of magnetite/dextran nanocomposite used as a precursor of magnetic fluid. *Chem Eng J* 150: 572–580.
32. Lin CL, Lee CF, Chiu WY (2005) Preparation and properties of poly(acrylic acid) oligomer stabilized superparamagnetic ferrofluid. *J Colloid Interf Sci* 291: 411–420.
33. Lin MM, Li SH, Kim HH, et al. (2010) Complete separation of magnetic nanoparticles via chemical cleavage of dextran by ethylenediamine for intracellular uptake. *J Mater Chem* 20: 444–447.
34. Lin JJ, Chen JS, Huang SJ, et al. (2009) Folic acid-Pluronic F127 magnetic nanoparticle clusters for combined targeting, diagnosis, and therapy applications. *Biomaterials* 30: 5114–5124.

35. Gupta AK, Gupta M (2005) Synthesis and surface engineering of iron oxide nanoparticles for biomedical applications. *Biomaterials* 26: 3995–4021.
36. Kuzminski M, Slawska-Waniewska A, Lachowicz HK (1999) The influence of superparamagnetic particle size distribution and ferromagnetic phase on GMR in melt spun Cu-Co granular alloys. *Ieee T Magn* 35: 2853–2855.
37. Yamashita T, Hayes P (2008) Analysis of XPS spectra of Fe^{2+} and Fe^{3+} ions in oxide materials. *Appl Surf Sci* 254: 2441–2449.
38. Barandeh F, Nguyen PL, Kumar R, et al. (2012) Organically modified silica nanoparticles are biocompatible and can be targeted to neurons in vivo. *PLoS One* 7: e29424.
39. Thuen M, Olsen O, Berry M, et al. (2009) Combination of Mn^{2+}-enhanced and diffusion tensor MR imaging gives complementary information about injury and regeneration in the adult rat optic nerve. *J Magn Reson Imaging* 29: 39–51.
40. Liu W, Frank JA (2008) Detection and quantification of magnetically labeled cells by cellular MRI. *Eur J Radiol* 70: 258–264.
41. Watanabe T, Radulovic J, Spiess J, et al. (2004) In vivo 3D MRI staining of the mouse hippocampal system using intracerebral injection of $MnCl_2$. *Neuroimage* 22: 860–867.
42. Gilad AA, Walczak P, McMahon MT, et al. (2008) MR tracking of transplanted cells with "positive contrast" using manganese oxide nanoparticles. *Magn Reson Med* 60: 1–7.
43. Hsiao JK, Tsai CP, Chung TH, et al. (2008) Mesoporous silica nanoparticles as a delivery system of gadolinium for effective human stem cell tracking. *Small* 4: 1445–1452.
44. Sumner JP, Shapiro EM, Maric D, et al. (2009) In vivo labeling of adult neural progenitors for MRI with micron sized particles of iron oxide: quantification of labeled cell phenotype. *Neuroimage* 44: 671–678.
45. Muldoon LL, Sandor M, Pinkston KE, et al. (2005) Imaging, distribution, and toxicity of superparamagnetic iron oxide magnetic resonance nanoparticles in the rat brain and intracerebral tumor. *Neurosurgery* 57: 785–796.
46. Lewinski N, Colvin V, Drezek R (2008) Cytotoxicity of nanoparticles. *Small* 4: 26–49.
47. Cosker KE, Courchesne SL, Segal RA (2008) Action in the axon: generation and transport of signaling endosomes. *Curr Opin Neurobiol* 18: 270–275.
48. Cui B, Wu C, Chen L, et al. (2007) One at a time, live tracking of NGF axonal transport using quantum dots. *P Natl Acad Sci USA* 104: 13666–13671.
49. Ha J, Lo KW, Myers KR, et al. (2008) A neuron-specific cytoplasmic dynein isoform preferentially transports TrkB signaling endosomes. *J Cell Biol* 181: 1027–1039.
50. Lenz JH, Schuchardt I, Straube A, et al. (2006) A dynein loading zone for retrograde endosome motility at microtubule plus-ends. *EMBO J* 25: 2275–2286.
51. Dhanikula RS, Argaw A, Bouchard JF, et al. (2008) Methotrexate loaded polyether-copolyester dendrimers for the treatment of gliomas: enhanced efficacy and intratumoral transport capability. *Mol Pharm* 5: 105–116.
52. Jeong YI, Seo SJ, Park IK, et al. (2005) Cellular recognition of paclitaxel-loaded polymeric nanoparticles composed of poly(gamma-benzyl L-glutamate) and poly(ethylene glycol) diblock copolymer endcapped with galactose moiety. *Int J Pharm* 296: 151–161.
53. Lu W, Sun Q, Wan J, et al. (2006) Cationic albumin-conjugated pegylated nanoparticles allow gene delivery into brain tumors via intravenous administration. *Cancer Res* 66: 11878–11887.

54. Howarth M, Takao K, Hayashi Y, et al. (2005) Targeting quantum dots to surface proteins in living cells with biotin ligase. *P Natl Acad Sci USA* 102: 7583–7588.
55. Zhang QZ, Zha LS, Zhang Y, et al. (2006) The brain targeting efficiency following nasally applied MPEG-PLA nanoparticles in rats. *J Drug Target* 14: 281–290.
56. Slotkin JR, Chakrabarti L, Dai HN, et al. (2007) In vivo quantum dot labeling of mammalian stem and progenitor cells. *Dev Dyn* 236: 3393–3401.
57. Gao X, Chen J, Wu B, et al. (2008) Quantum dots bearing lectin-functionalized nanoparticles as a platform for in vivo brain imaging. *Bioconjug Chem* 19: 2189–2195.
58. Santra S, Yang H, Holloway PH, et al. (2005) Synthesis of water-dispersible fluorescent, radio-opaque, and paramagnetic CdS: Mn/ZnS quantum dots: a multifunctional probe for bioimaging. *J Am Chem Soc* 127: 1656–1657.
59. Wang J, Chen C, Liu Y, et al. (2008) Potential neurological lesion after nasal instillation of TiO_2 nanoparticles in the anatase and rutile crystal phases. *Toxicol Lett* 183: 72–80.
60. Tang M, Xing T, Zeng J, et al. (2008) Unmodified CdSe quantum dots induce elevation of cytoplasmic calcium levels and impairment of functional properties of sodium channels in rat primary cultured hippocampal neurons. *Environ Health Persp* 116: 915–922.
61. Sayes CM, Gobin AM, Ausman KD, et al. (2005) Nano-C60 cytotoxicity is due to lipid peroxidation. *Biomaterials* 26: 7587–7595.
62. Liu G, Hong RY, Guo L, et al. (2011) Preparation, characterization and MRI application of carboxymethyl dextran coated magnetic nanoparticles. *Appl Surf Sci* 257: 6711–6717.

AIMS Press